Journal of Materials Chemistry A

PAPER

View Article Online
View Journal | View Issue

Cite this: J. Mater. Chem. A, 2016, 4, 17749

Preparation of a hybrid $Cu_2O/CuMoO_4$ nanosheet electrode for high-performance asymmetric supercapacitors†

Dongwei Du,[a] Rong Lan,[a] Wei Xu,[a] Richard Beanland,[b] Huanting Wang[c] and Shanwen Tao*[ac]

Received 6th October 2016
Accepted 24th October 2016

DOI: 10.1039/c6ta08670e

www.rsc.org/MaterialsA

Supercapacitors have attracted considerable attention due to their fast charge–discharge ability, excellent rate capability and long-term stability. In this study, a novel electrode composed of $Cu_2O/CuMoO_4$ nanosheets directly grown on Ni foam was synthesized *via* a facile hydrothermal method. The as-prepared electrode exhibits remarkably improved specific and areal capacitance (up to 4264 F g^{-1} and 9.38 F cm^{-2} at a current density of 1 A g^{-1}). To the best of our knowledge, the specific capacitance of 4264 F g^{-1} is the highest in reported studies although the areal capacitance of 9.38 F g^{-1} is slightly lower than the highest value of 16 F cm^{-2} when $Ni(OH)_2$/carbon nanotubes on Ni foam was used as the electrode. An asymmetric supercapacitor is fabricated using the $Cu_2O/CuMoO_4$ nanosheet electrode as the positive electrode and activated carbon (AC) as the negative electrode. The operation voltage could expand to 1.7 V, at which the energy density can reach 75.1 W h kg^{-1} with a power density of 420 W kg^{-1}. Additionally, the asymmetric supercapacitor exhibits very high rate capability and good cycling stability. The capacitance remains around 86.6% after 3000 cycles at a current density of 5 A g^{-1}. This indicates that the $Cu_2O/CuMoO_4$ nanosheet electrode is promising for applications in renewable energy storage in the future.

1. Introduction

Energy and power demands keep increasing year by year due to the fast development of the world. Traditional energy supply is mainly based on the combustion of fossil fuels which causes many environmental issues. To avoid and address these problems, many researchers have started to develop alternative energy storage and conversion systems. The electrochemical capacitor (EC), also called supercapacitor, as one of the promising new classes of energy storage devices, has attracted significant interest due to its rapid charge–discharge rate, high power density and long life span.[1–6] Presently, most commercial supercapacitors are symmetric and carbon material-based, which are known as electric double layer capacitors (EDLCs).[7–9] The carbon-based material usually has low energy density which restricts its further application compared to batteries.[10,11] Therefore, it is necessary to develop high quality supercapacitors with improved energy density without sacrificing the power density. Asymmetric capacitors are considered as one of the best alternatives because the redox reactions during charge–discharge processes can lead to larger specific capacitance.[12,13] In a typical asymmetric supercapacitor, one electrode is derived from carbon-based materials while the other one is made of pseudocapacitive materials. It can combine the advantages of the two types of materials to exhibit high operating potential, and achieve high energy density. The performances of asymmetric supercapacitors are determined by the properties of the specific electrode materials. Therefore, it is important to develop novel pseudocapacitive materials.

Many efforts have been made to explore the pseudocapacitive materials for supercapacitors, and transition-metal oxides/hydroxides are the commonly used materials.[14–17] In particular, mixed metal oxides/hydroxides usually offer better electrical performances because of their improved conductivity as well as their synergic effects.[18–22] For example, Liu *et al.* found that $CoMoO_4$–$NiMoO_4$ exhibited higher specific capacitance than $CoMoO_4$ and better rate capability than $NiMoO_4$.[23] Similarly, the investigation on Co–Ni double hydroxides has proved that the hybrid hydroxide electrodes significantly outperform either $Co(OH)_2$ or $Ni(OH)_2$ alone.[24–26] Nevertheless, the performance of pseudocapacitive materials still suffers from intrinsic poor electric conductivity and insufficient diffusion of the electrolyte into the active materials, namely, a large portion of the active materials are not

[a]School of Engineering, University of Warwick, Coventry CV4 7AL, UK. E-mail: S.Tao.1@warwick.ac.uk

[b]Department of Physics, University of Warwick, Coventry CV4 7AL, UK

[c]Department of Chemical Engineering, Monash University, Clayton, Victoria 3800, Australia

† Electronic supplementary information (ESI) available: SEM image, EDS analysis, CV and charge/discharge curves and other additional supporting data. See DOI: 10.1039/c6ta08670e

accessible to the electrolyte to undergo faradaic reactions during the charge–discharge process thus no contribution to the specific capacitance.[27] Developing nanostructured materials with a large surface area is regarded as an effective strategy to overcome these issues. In addition, directly growing the active materials on the conductive substrate can reduce internal resistance and make full use of the active materials, therefore improving the capacitance and stability.[28–30] Among different oxide materials for supercapacitors, copper oxides have drawn much attention in supercapacitors due to their low cost, environmental benignity and abundance.[31–33] Shinde *et al.* prepared 3D-flower-like CuO on copper foil which exhibited 498 F g^{-1} at 5 mV s^{-1}.[34] Wang *et al.* measured the properties of CuO nanosheets, and a capacity of 569 F g^{-1} was obtained at a current density of 5 mA cm^{-2} in 6.0 M KOH electrolyte.[35] However, it is still a big challenge for commercial utilisation of Cu oxide supercapacitors, and more studies should be conducted to achieve the commercial requirements. By combining the aforementioned strategies, it can be deduced that better performance would be obtained if nanostructured copper oxide hybrids can be directly grown on conductive substrates. On the other hand, to the best of our knowledge, the application of $CuMoO_4$ for supercapacitors has not been reported. Herein, $Cu_2O/CuMoO_4$ nanosheets directly grown on Ni foam have been synthesized. The as-prepared electrode exhibits high specific and areal capacitance and also displays good rate capability. In addition, excellent electrical performances are obtained in the asymmetric supercapacitor with AC as the negative electrode. An energy density of 75.1 W h kg^{-1} and a power density of 420 W kg^{-1} can be achieved with the voltage window at 1.7 V. Taking the fascinating performances and easy fabrication procedures into account, the hybrid $Cu_2O/CuMoO_4$ nanosheet electrode is promising for commercial application in high-energy storage in the future.

2. Experimental section

2.1. Preparation of hybrid $Cu_2O/CuMoO_4$ nanosheets on Ni foam

All the reagents were used without further purification. $Cu_2O/CuMoO_4$ nanosheets were synthesized by a facile hydrothermal method. Prior to the synthesis, the Ni foam (1 × 1 cm^2) was cleaned by ultra-sonication in 2 M HCl solution, ethanol and deionized water for several minutes, respectively. The solution containing 0.05 M $Cu(NO_3)_2$ and 0.05 M Na_2MoO_4 was obtained by dissolving copper(II) nitrate hemi(pentahydrate) and sodium molybdate dihydrate in deionized water under constant stirring. The prepared solution was transferred into a Teflon lined stainless steel autoclave. Ni foam was immersed in the homogeneous solution, and then the autoclave was heated at 160 °C for 15 h and naturally cooled down to room temperature. The Ni foam was taken out and washed with water and ethanol to remove surface ions and molecules, and then followed by drying at 60 °C overnight in a vacuum oven. Finally, the Ni foam with the as-grown hydrate precursors was calcined at 450 °C for 2 h in an argon atmosphere with a heating rate of 1 °C min^{-1}. The mass loading of the active materials was obtained by comparing the weight of the Ni foam before the hydrothermal reaction and after the calcination, which was determined to be around 2.2 mg cm^{-2}. For the sake of comparison, the precursor solution without Na_2MoO_4 was applied to fabricate electrodes by the same process.

2.2. Assembly of the $Cu_2O/CuMoO_4$//AC asymmetric supercapacitor

To fabricate the asymmetric supercapacitor, the as-prepared $Cu_2O/CuMoO_4$ electrode was used as the positive electrode and an activated carbon (AC) electrode acted as the negative electrode. The AC electrode was obtained by mixing the activated carbon (Black Pearl 2000, Cabot) and polytetrafluoroethylene at a mass ratio of 95 : 5 in water under constant magnetic stirring. The prepared slurry was spread onto a Ni foam (1 × 1 cm^2) and then pressed and dried at 60 °C overnight under vacuum. The mass ratio of $Cu_2O/CuMoO_4$ nanosheets and AC was optimized to be around 2.2 and 5.6 mg cm^{-2}. To assemble the full cell, the negative electrode and positive electrode were placed face-to-face into a container in which 2 M KOH was added as the electrolyte.

2.3. Physical characterization

X-ray Diffraction (XRD) was carried out to identify the crystal structures on a Panalytical X'Pert Pro Multi-Purpose Diffractometer (MPD) with Cu Kalpha1 radiation working at 45 kV and 40 mA. Scanning electron microscopy (SEM) (ZEISS SUPRA 55-VP) and transmission electron microscopy (TEM) (JEOL 2100) were applied to observe the morphologies. Energy-dispersive X-ray spectroscopy (EDX) attached to the SEM was employed to analyze the elemental compositions.

2.4. Electrochemical measurements

The electrochemical properties of the as-prepared $Cu_2O/CuMoO_4$ and AC electrodes were studied in a conventional three-electrode cell configuration. In particular, the as-obtained electrode ($Cu_2O/CuMoO_4$ or AC) was used as the working electrode. The working electrode was soaked in 2 M KOH for 2 days and activated for 1000 cyclic voltammetry (CV) loops before the test. A piece of Pt mesh (1 × 1 cm^2) and an Ag/AgCl electrode (sat. KCl) were used as counter and reference electrodes, respectively. The electrochemical performances of the asymmetric supercapacitor were explored in a two-electrode mode in which $Cu_2O/CuMoO_4$ acted as the positive electrode while the AC electrode was used as the negative electrode. All the measurements were performed in 2 M KOH solution at room temperature and recorded on a Solartron 1470E multichannel cell test system. The a.c. impedance was recorded at open circuit voltage by using an integrated Solartron 1455 frequency response analyzer at 5 mV bias with a frequency range of 100 kHz to 0.01 Hz.

2.5. Calculations

The specific capacitance of the electrode in three-electrode mode was calculated from the galvanostatic charge–discharge curves according to the following equation:[19,36]

$$C_s = \frac{I \times \Delta t}{m_1 \times \Delta V} \text{ or } \frac{I \times \Delta t}{A \times \Delta V} \quad (1)$$

where C_s is the specific capacitance (F g^{-1} or F cm^{-2}), I is the discharge current (A), Δt is the discharge time (s), m is the mass of the active materials on the Ni foam (g), ΔV is the potential change excluding the IR drop in the discharge step (V), and A is the geometric area of the electrode (cm^2). In terms of the specific capacitance of the asymmetric supercapacitor, it was also calculated from the galvanostatic charge–discharge curves with the same formula:[37,38]

$$C_s = \frac{I \times \Delta t}{m_2 \times \Delta V} \quad (2)$$

where m_2 is the total mass of the active materials in positive and negative electrodes (g).

The energy densities and power densities of the asymmetric supercapacitor were obtained by the following equations:[37,38]

$$E = \frac{1}{2} C_s V^2 \times \frac{1}{3.6} \quad (3)$$

$$P = 3600 \times \frac{E}{\Delta t} \quad (4)$$

where E is the energy density (W h kg^{-1}), C_s is the specific capacitance (F g^{-1}), V is the capacitor potential window excluding the IR drop (V), P is the power density (W kg^{-1}) and Δt is the discharge time (s).

3. Results and discussion

3.1. Physical characterization of the electrode

Fig. 1a–d show the scanning electron microscopy (SEM) images of the $Cu_2O/CuMoO_4$ supported on Ni foam at different magnifications. The Ni foam shows a nice 3D porous structure (Fig. S1, ESI†) and its surface is flat and clean after acid treatment (Fig. S1b and c, ESI†). However, the images at low magnification (Fig. 1a and b) indicate that the Ni foam surface becomes rough after the synthesis procedure as plenty of materials are deposited on it, which proves that the applied hydrothermal process can facilitate growing materials on the substrate. From the enlarged pictures (Fig. S1c and d†), it can be seen that nanosheet clusters are uniformly distributed on the surface forming a grass-like morphology. Moreover, the nanosheets are interconnected with each other ultimately producing porous texture. Thus, a large surface area is generated and most of the nanosheet surface could be easily accessed by the electrolyte during the electrochemical test. It should be noted that the electrode was washed and calcined after the hydrothermal process; the overall nanostructure is still well defined, which indicates excellent stability. Fig. S2 (ESI†) shows the surface structures of Cu_2O grown on Ni foam when only $Cu(NO_3)_2$ was used as the precursor solution. Obviously the surface is covered by grain shaped crystals with the size of around 10 μm. The difference in microstructures between the two samples reveals that the addition of MoO_4^{2-} can significantly affect the growth process, facilitating the formation of nanosheets.

To identify the elemental compositions of the materials grown on Ni foam, energy-dispersive X-ray spectroscopy (EDX) analysis has been conducted on the electrode and the results are shown in Fig. S3 and S4 (ESI†). The EDX spectrum indicates that the nanosheets are composed of Ni, Cu, Mo, and O elements (Fig. S3a, ESI†), which is also confirmed by the EDX mapping (Fig. S3c–f, ESI†). Besides the Ni signal derived from Ni foam, the results are consistent with those of the raw materials used in the hydrothermal reaction.

The compositions of the grown materials are also identified by X-ray diffraction (XRD). No impurities are detected on the Ni foam substrate except the Ni peaks (Fig. S5a, ESI†). As shown in Fig. 2, the background of the Ni foam is very strong but the

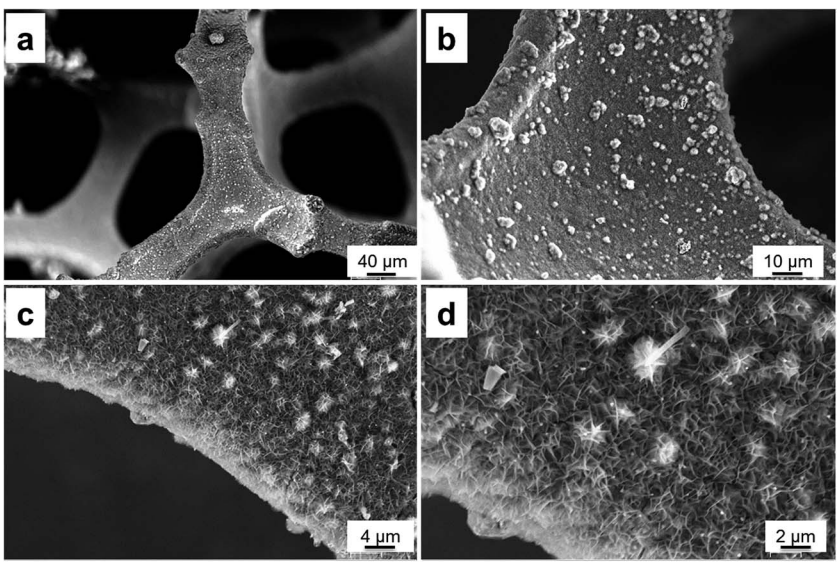

Fig. 1 Typical SEM images of $Cu_2O/CuMoO_4$ nanosheets on Ni foam at different magnifications.

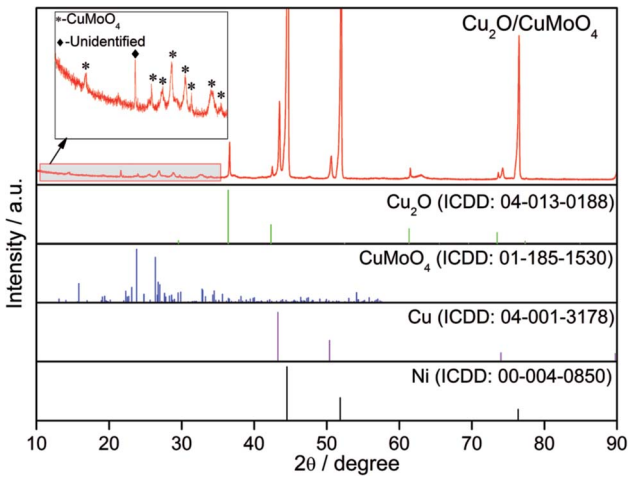

Fig. 2 XRD patterns of the as-synthesized electrode.

diffraction patterns still reveal that the composition of the grown materials is the hybrid of Cu_2O, $CuMoO_4$ and Cu as the remaining peaks can be assigned to the standard Cu_2O (ICDD 04-013-0188), $CuMoO_4$ (ICD 00-047-0511) and Cu (ICDD: 00-004-0850). In terms of the sample prepared with only $Cu(NO_3)_2$ as precursor solution (Fig. S5b, ESI†), Cu_2O and Cu were detected. A peak at $2\theta \approx 27.1^\circ$ was not identified, which needs further investigation. The $CuMoO_4$ phase was not well crystallised, and its existence is further confirmed by transmission electron microscopy (TEM) (Fig. 3). The high-resolution TEM (HRTEM) images with lattice fringes are presented in Fig. 3a and b, and the corresponding Fourier transform patterns (inset of Fig. 3b) demonstrate the interplanar distance around 0.457, 0.379, 0.399, 0.408 and 0.512 nm, which can be indexed to the (110), (201), ($\bar{1}02$), (002) and ($1\bar{1}1$) planes of $CuMoO_4$. It can be deduced that during the hydrothermal process, a portion of Cu^{2+} ions are converted into Cu_2O and Cu, while the addition of MoO_4^{2-} ions can simultaneously produce $CuMoO_4$. It is known that Cu would be electro-oxidized to Cu_2O in the KOH electrolyte by employing cyclic voltammetry (CV);[31,38] therefore the electrolyte accessible Cu on the Ni foam is converted to Cu_2O after the activation step while the remaining Cu can function as a part of the current collector to improve the electrode conductivity. The active materials here are therefore denoted as $Cu_2O/CuMoO_4$.

3.2. Electrochemical performances of the hybrid $Cu_2O/CuMoO_4$ nanosheet electrode

To evaluate the electrochemical performances of the $Cu_2O/CuMoO_4$ nanosheet electrode, the synthesized electrode was measured in a three-electrode cell configuration in 2 M KOH aqueous solution. It should be noted that the Ni foam substrate contributes negligible capacitance under the conditions in this work. The CV curves of the bare Ni foam electrode (1×1 cm^2, calculated as 1 mg), Cu_2O grown on Ni foam and hybrid $Cu_2O/CuMoO_4$ nanosheet electrode at 1 mV s^{-1} are compared in Fig. S6 (ESI†), it is obvious that the current density on the bare Ni foam and Cu_2O electrodes are far lower than it on the $Cu_2O/CuMoO_4$ nanosheet electrode. The CV curves of $Cu_2O/CuMoO_4$ at different scan rates from 1 to 20 mV s^{-1} are shown in Fig. 4a. The appearance of distinct redox peaks between 0 and 0.6 V *vs.* Ag/AgCl confirms the pseudocapacitive behaviour of the materials and implies good electrochemical reversibility. Obviously, the current density increases with increasing scan rate, while the anodic and cathodic peaks slightly shift towards the more positive and negative potentials respectively, which is supposed to be related to the internal resistance of the electrode[38] and limitation of charge transfer kinetics.[27] Fig. 4b shows the galvanostatic charge–discharge curves at various current densities from 1 to 50 A g^{-1}. The nonlinear charge–discharge profiles further support the pseudocapacitive characteristics of the electrode, which is in good agreement with the CV curves as shown in Fig. 4a. Based on the discharge curves, the corresponding specific and areal capacitances are calculated (Fig. 4c). The specific capacitance is 4264 F g^{-1} (9.38 F cm^{-2}) at a current density of 1 A g^{-1}, and it decreases to 3121 F g^{-1} (6.87 F cm^{-2}) when the current density increases to 10 A g^{-1}. To the best of our knowledge, the specific capacitance of 4264 F g^{-1} is the highest in reported studies although the areal capacitance of 9.38 F g^{-1} is slightly lower than the highest value of 16 F cm^{-2} when $Ni(OH)_2$/carbon nanotubes on Ni foam was used as the electrode.[39] It is believed that the degradation of capacitance

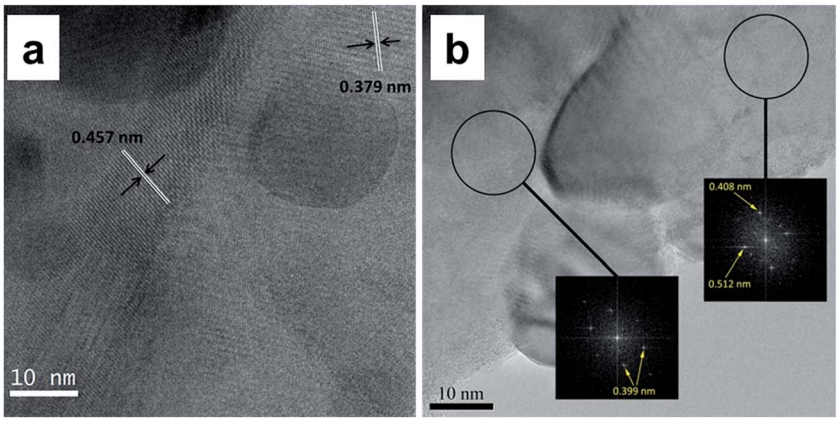

Fig. 3 (a and b) TEM images of $Cu_2O/CuMoO_4$ nanosheets and the corresponding Fourier transform patterns (inset of b).

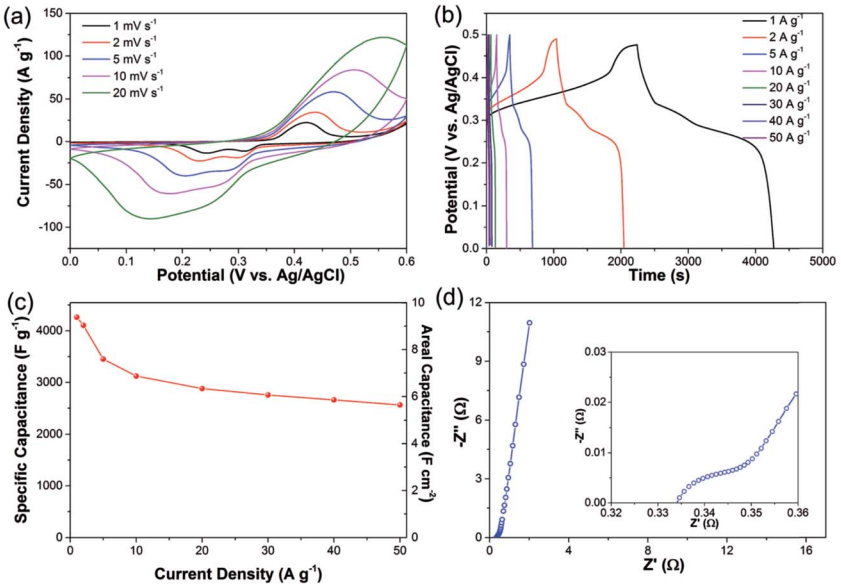

Fig. 4 (a) CV curves of the $Cu_2O/CuMoO_4$ nanosheet electrode at different scan rates. (b) Galvanostatic charge–discharge curves of the $Cu_2O/CuMoO_4$ electrode at various current densities. (c) Specific and areal capacitances at various current densities. (d) Nyquist plots of the $Cu_2O/CuMoO_4$ electrode recorded at open circuit potential in the frequency range of 100 kHz to 0.01 Hz. The inset of (d) shows the impedance in the high-frequency region.

with the increase of the current densities is mainly due to the incremental IR drop and insufficient active material involved in redox reactions at higher current densities.[27] However, as the current density keeps increasing, the electrode exhibits remarkable rate capability, namely, the capacitance still remains at 2563 F g^{-1} (5.64 F cm^{-2}) at a current density as high as 50 A g^{-1}. The capacitance values presented here are much higher than those reported in previous studies using similar materials: Cu_2O/Cu nanoneedle arrays (510.2 F g^{-1}, 0.88 F cm^{-2} at 2.9 A g^{-1});[38] mesoporous NiO nanosheets (2504.3 F g^{-1}, 0.376 F cm^{-2} at 13.4 A g^{-1});[37] $NiMoO_4$ nanowires (3298 F g^{-1}, 4.94 F cm^{-2} at 5.33 A g^{-1});[27] $MnCo_2O_4/Ni(OH)_2$ core–shell nanoflowers (2124 F g^{-1}, 3.19 F cm^{-2} at 5 A g^{-1});[19] $NiCoO_2$ (508 F g^{-1} at 0.5 A g^{-1}).[40] To further investigate the electrochemical behavior of the $Cu_2O/CuMoO_4$ electrode, electrochemical impedance spectroscopy (EIS) measurement is carried out in the frequency range from 100 kHz to 0.01 Hz at open circuit potential with the amplitude at 5 mV. As shown in Fig. 4d, the Nyquist plots of the $Cu_2O/CuMoO_4$ electrode are composed of a semicircle in the high-frequency region and a linear component in the low-frequency region. The intercept of the plots at the real axis represents the equivalent series resistance (R_s), including the ionic resistance of the electrolyte, intrinsic resistance of active materials and the contact resistance between the active materials and current collector,[41–43] which is determined to be 0.334 Ω (inset of Fig. 4d). In terms of the semicircle, its diameter indicates the charge transfer resistance (R_{ct}) of the system.[41–43] The corresponding R_{ct} of the $Cu_2O/CuMoO_4$ electrode is only 0.02 Ω, implying the easy and rapid charge transfer on the electrode. In the low-frequency region, the straight line presents the Warburg impedance (Z_w),[41–43] associated with the diffusion of the electrolyte ions along the $Cu_2O/CuMoO_4$ nanosheets. The large slope of the straight line shown in Fig. 4d demonstrates a very small Z_w of the electrolyte ion diffusion. The small values of R_s, R_{ct} and Z_w suggest that there is a large electro-active surface area and higher electrical conductivity with the $Cu_2O/CuMoO_4$ nanosheet, which could extend the reaction zone of the electrode, making more electrode materials available for the charging/discharging process, leading to high capacitance.

The dramatic high capacitance and outstanding rate capability of the $Cu_2O/CuMoO_4$ hybrid electrode can be attributed to its synthesis technique, nanostructure, and the possible synergistic effect from Cu_2O and $CuMoO_4$. The active materials are directly grown on the Ni foam current collector without any binders and conductive additives, which greatly reduces the contact resistance and improves the electrical conductivity of each nanosheet, leading to excellent conductivity of the electrode. Additionally, the specific surface area is significantly expanded with the nanosheets, which not only increases the electrolyte/electrode contact areas but also creates more active sites for rapid redox reactions with the anions and water molecules, enhancing the utilization of the $Cu_2O/CuMoO_4$. Moreover, the nanostructure could effectively facilitate the transport of electrolyte ions and electrons, and simultaneously, it is compatible with larger volume changes during the fast surface-dependent faradaic processes.

3.3. Electrochemical performances of the $Cu_2O/CuMoO_4$// AC asymmetric supercapacitor

An asymmetric supercapacitor was assembled using the prepared $Cu_2O/CuMoO_4$ electrode as the positive electrode and the AC electrode as the negative electrode for further investigating the performances of the $Cu_2O/CuMoO_4$ nanosheet

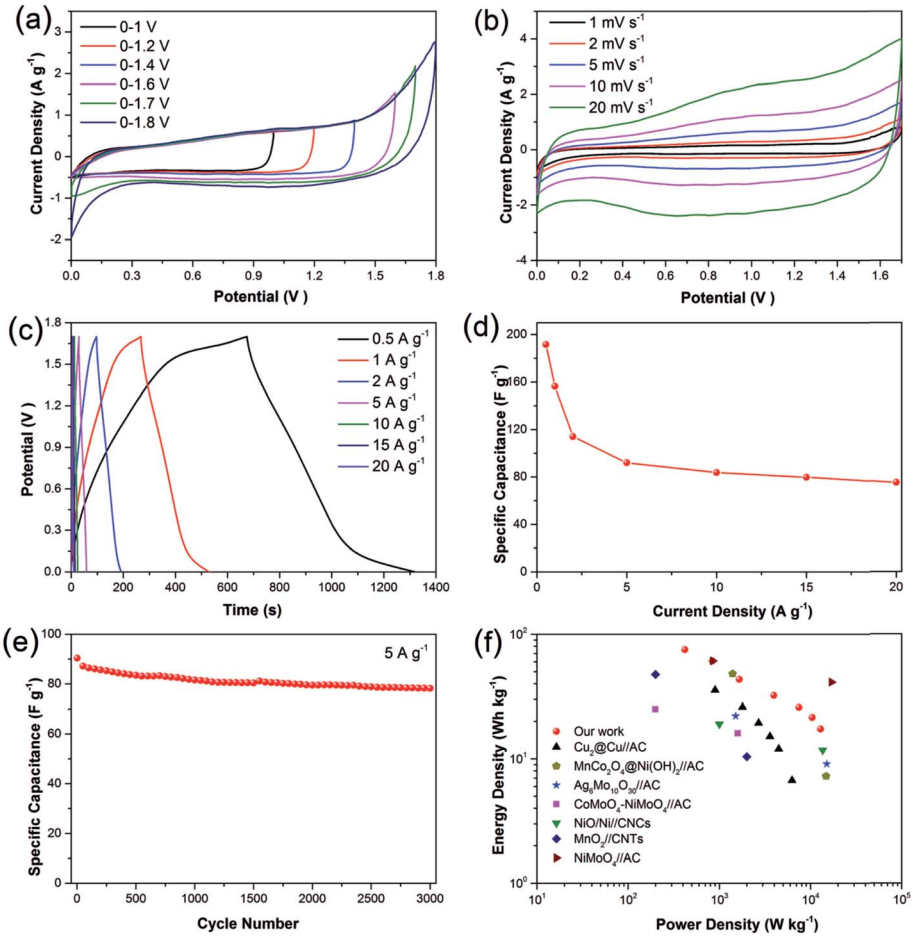

Fig. 5 Electrochemical properties of the $Cu_2O/CuMoO_4$//AC asymmetric supercapacitor: (a) CV curves in various voltage windows at 5 mV s^{-1}; (b) CV curves with a voltage window of 0–1.7 V at various scan rates; (c) galvanostatic charge–discharge curves at various current densities; (d) specific capacitance at various current densities. (e) Cycling performances of the asymmetric supercapacitor for 3000 cycles at 5 A g^{-1}; (f) Ragone plots of our supercapacitor, compared with some other supercapacitors reported previously (CNCs: carbon nanocages and CNTs: carbon nanotubes).

electrode under practical conditions. The electrochemical performance of AC presents a typical feature of carbon-based materials (see Fig. S7, ESI†). In order to find the optimal working potential, a series of CV measurements in different voltage windows were conducted at 5 mV s^{-1}. As seen from Fig. 5a, the operating windows are stable from 1.0 to 1.7 V. When it reaches 1.8 V, the polarization trend becomes very obvious, which means that severe water electrolysis happens. Therefore the best operating voltage window is determined to be 1.7 V. Fig. 5b presents the CV performances of the asymmetric supercapacitor at different scan rates ranging from 1 to 20 mV s^{-1}. Unlike the single $Cu_2O/CuMoO_4$ or AC electrode, the asymmetric supercapacitor shows quasi-rectangular CV curves in all scans, which means that the capacitance is derived from both electric double-layer capacitance and pseudocapacitance. The operation voltage of 1.7 V here should be dependent on this remarkable synergy effect. The galvanostatic charge–discharge curves of the asymmetric supercapacitor were recorded at the

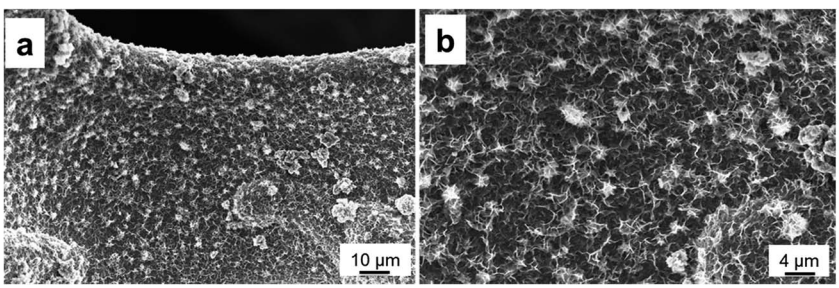

Fig. 6 SEM images of the $Cu_2O/CuMoO_4$ nanosheet electrode after charge–discharge for 3000 cycles at a current density of 5 A g^{-1}.

current densities from 0.5 to 20 A g^{-1} (Fig. 5c). It can be seen that the discharge curves are nonlinear especially at low current densities, indicating the double contribution of electric double-layer capacitance and pseudocapacitance, which is consistent with the CV results. Based on the total mass of the positive and negative electrodes, the specific capacitance at various current densities is plotted in Fig. 5d. The calculated capacitances are 191, 156, 114, 92, 83.7, 79.8 and 75.1 F g^{-1} at current densities of 0.5, 1, 2, 5, 10, 15 and 20 A g^{-1}, respectively. It can be found that the as-fabricated asymmetric supercapacitor reveals excellent rate capability from 5 to 20 A g^{-1}. To further investigate the durability of the asymmetric supercapacitor, its cycling performance was recorded at 5 A g^{-1} (Fig. 5e). The specific capacitance still retains 86.6% of the initial value even after 3000 cycles, which demonstrates excellent electrochemical stability. It is believed the decline of the capacitance is caused by the destruction of the electrode film under numerous rapid redox reactions.[19] This is also evidenced by first and last ten charge–discharge curves (Fig. S8, ESI†).

The Ragone plots of the asymmetric supercapacitor derived from the discharge curve based on eqn (3) and (4) are displayed in Fig. 5f. The maximum energy density can be determined to be 75.1 W h kg^{-1} at the average power density of 420 W kg^{-1}. It can still maintain 21.5 W h kg^{-1} even at a high power density of 10 435 W kg^{-1}. It is found that the performance of the $Cu_2O/CuMoO_4$//AC asymmetric supercapacitor is better than that of many previously reported systems, such as Cu_2O@Cu//AC,[38] $MnCo_2O_4$@$Ni(OH)_2$//AC,[19] $Ag_6Mo_{10}O_{30}$//AC,[44] $CoMoO_4$–$NiMoO_4$//AC,[23] NiO/Ni//CNCs[45] and MnO_2//CNTs[46] but a higher energy density at 41.1 W h kg^{-1} was achieved with the power density of 17 002 W kg^{-1} by a $NiMoO_4$//AC system.[20]

To further probe the stability of the hybrid electrode, the sample after the stability test was observed by SEM. Fig. 6 presents the SEM images after 3000 charge–discharge cycles at 5 A g^{-1}; it can be clearly seen that the physical microstructures of the electrode maintain very well, which are still in nanosheets. As no notable changes can be found on the electrode before and after the cycling measurements, it proves the good stability of the hybrid electrode.

4. Conclusions

In summary, we synthesized a hybrid $Cu_2O/CuMoO_4$ nanosheet electrode *via* a facile hydrothermal method and it exhibits remarkably improved specific and areal capacitance (up to 4264 F g^{-1} and 9.38 F cm^{-2} at a current density of 1 A g^{-1}). To the best of our knowledge, the specific capacitance of 4264 F g^{-1} is the highest in reported studies although the areal capacitance of 9.38 F g^{-1} is slightly lower than the highest value of 16 F cm^{-2} when $Ni(OH)_2$/carbon nanotubes on Ni foam was used as the electrode. In addition, the electrode presents good rate capability; specifically, the capacitance still retains 2563 F g^{-1} (5.64 F cm^{-2}) at a current density as high as 50 A g^{-1}. Moreover, an asymmetric supercapacitor is fabricated using the $Cu_2O/CuMoO_4$ nanosheet electrode as the positive electrode and AC as the negative electrode. The operation voltage of the asymmetric supercapacitor could achieve 1.7 V, at which the energy density is 75.1 W h kg^{-1} with a power density of 420 W kg^{-1}. The asymmetric supercapacitor also displays excellent rate capability and cycling stability. The capacitance remains around 86.6% after 3000 cycles at a current density of 5 A g^{-1}. Considering the fascinating performances of $Cu_2O/CuMoO_4$ nanosheet electrodes and easy fabrication procedures, the electrodes are promising for applications in renewable energy storage.

Acknowledgements

One of the authors (Du) thanks the University of Warwick for a PhD studentship.

References

1 J. Bae, M. K. Song, Y. J. Park, J. M. Kim, M. Liu and Z. L. Wang, *Angew. Chem., Int. Ed.*, 2011, **50**, 1683–1687.
2 N. Yu, H. Yin, W. Zhang, Y. Liu, Z. Tang and M. Q. Zhu, *Adv. Energy Mater.*, 2016, **6**, DOI: 10.1002/aenm.201501458.
3 J. Wu, X. Gao, H. Yu, T. Ding, Y. Yan, B. Yao, X. Yao, D. Chen, M. Liu and L. Huang, *Adv. Funct. Mater.*, 2016, **26**, 6114–6120.
4 G. Wang, L. Zhang and J. Zhang, *Chem. Soc. Rev.*, 2012, **41**, 797–828.
5 J. R. Miller and P. Simon, *Science*, 2008, **321**, 651–652.
6 J. Liu, L. Zhang, H. B. Wu, J. Lin, Z. Shen and X. W. D. Lou, *Energy Environ. Sci.*, 2014, **7**, 3709–3719.
7 Y. Zhu, S. Murali, M. D. Stoller, K. Ganesh, W. Cai, P. J. Ferreira, A. Pirkle, R. M. Wallace, K. A. Cychosz and M. Thommes, *Science*, 2011, **332**, 1537–1541.
8 P. Chen, J.-J. Yang, S.-S. Li, Z. Wang, T.-Y. Xiao, Y.-H. Qian and S.-H. Yu, *Nano Energy*, 2013, **2**, 249–256.
9 J.-S. M. Lee, T.-H. Wu, B. M. Alston, M. E. Briggs, T. Hasell, C.-C. Hu and A. I. Cooper, *J. Mater. Chem. A*, 2016, **4**, 7665–7673.
10 P. Simon, Y. Gogotsi and B. Dunn, *Science*, 2014, **343**, 1210–1211.
11 Z. Yu, L. Tetard, L. Zhai and J. Thomas, *Energy Environ. Sci.*, 2015, **8**, 702–730.
12 Z.-S. Wu, W. Ren, D.-W. Wang, F. Li, B. Liu and H.-M. Cheng, *ACS Nano*, 2010, **4**, 5835–5842.
13 Y.-Z. Su, K. Xiao, N. Li, Z.-Q. Liu and S.-Z. Qiao, *J. Mater. Chem. A*, 2014, **2**, 13845–13853.
14 Z. Lu, Z. Chang, W. Zhu and X. Sun, *Chem. Commun.*, 2011, **47**, 9651–9653.
15 T. Brezesinski, J. Wang, S. H. Tolbert and B. Dunn, *Nat. Mater.*, 2010, **9**, 146–151.
16 M. Huang, Y. Zhang, F. Li, L. Zhang, Z. Wen and Q. Liu, *J. Power Sources*, 2014, **252**, 98–106.
17 L. Yu, B. Guan, W. Xiao and X. W. D. Lou, *Adv. Energy Mater.*, 2015, **5**, DOI: 10.1002/aenm.201500981.
18 L. Bao, J. Zang and X. Li, *Nano Lett.*, 2011, **11**, 1215–1220.
19 Y. Zhao, L. Hu, S. Zhao and L. Wu, *Adv. Funct. Mater.*, 2016, **26**, 4085–4093.
20 S. Peng, L. Li, H. B. Wu, S. Madhavi and X. W. D. Lou, *Adv. Energy Mater.*, 2015, **5**, DOI: 10.1002/aenm.201401172.
21 D. Cai, D. Wang, B. Liu, L. Wang, Y. Liu, H. Li, Y. Wang, Q. Li and T. Wang, *ACS Appl. Mater. Interfaces*, 2014, **6**, 5050–5055.

22 L. Huang, D. Chen, Y. Ding, Z. L. Wang, Z. Zeng and M. Liu, *ACS Appl. Mater. Interfaces*, 2013, **5**, 11159–11162.
23 M.-C. Liu, L.-B. Kong, C. Lu, X.-J. Ma, X.-M. Li, Y.-C. Luo and L. Kang, *J. Mater. Chem. A*, 2013, **1**, 1380–1387.
24 X. Xiong, D. Ding, D. Chen, G. Waller, Y. Bu, Z. Wang and M. Liu, *Nano Energy*, 2015, **11**, 154–161.
25 H. Chen, L. Hu, M. Chen, Y. Yan and L. Wu, *Adv. Funct. Mater.*, 2014, **24**, 934–942.
26 Y. Cheng, H. Zhang, C. V. Varanasi and J. Liu, *Energy Environ. Sci.*, 2013, **6**, 3314–3321.
27 D. Guo, P. Zhang, H. Zhang, X. Yu, J. Zhu, Q. Li and T. Wang, *J. Mater. Chem. A*, 2013, **1**, 9024–9027.
28 M. Yu, J. Chen, J. Liu, S. Li, Y. Ma, J. Zhang and J. An, *Electrochim. Acta*, 2015, **151**, 99–108.
29 X. Yu, B. Lu and Z. Xu, *Adv. Mater.*, 2014, **26**, 1044–1051.
30 J. Jiang, J. Liu, W. Zhou, J. Zhu, X. Huang, X. Qi, H. Zhang and T. Yu, *Energy Environ. Sci.*, 2011, **4**, 5000–5007.
31 C. Dong, Q. Bai, G. Cheng, B. Zhao, H. Wang, Y. Gao and Z. Zhang, *RSC Adv.*, 2015, **5**, 6207–6214.
32 A. Pendashteh, M. F. Mousavi and M. S. Rahmanifar, *Electrochim. Acta*, 2013, **88**, 347–357.
33 K. Wang, C. Zhao, S. Min and X. Qian, *Electrochim. Acta*, 2015, **165**, 314–322.
34 S. K. Shinde, D. P. Dubal, G. S. Ghodake and V. Fulari, *RSC Adv.*, 2015, **5**, 4443–4447.
35 G. Wang, J. Huang, S. Chen, Y. Gao and D. Cao, *J. Power Sources*, 2011, **196**, 5756–5760.
36 Q. Lu, M. W. Lattanzi, Y. Chen, X. Kou, W. Li, X. Fan, K. M. Unruh, J. G. Chen and J. Q. Xiao, *Angew. Chem.*, 2011, **123**, 6979–6982.
37 G. Cheng, W. Yang, C. Dong, T. Kou, Q. Bai, H. Wang and Z. Zhang, *J. Mater. Chem. A*, 2015, **3**, 17469–17478.
38 C. Dong, Y. Wang, J. Xu, G. Cheng, W. Yang, T. Kou, Z. Zhang and Y. Ding, *J. Mater. Chem. A*, 2014, **2**, 18229–18235.
39 Z. Tang, C. H. Tang and H. Gong, *Adv. Funct. Mater.*, 2012, **22**, 1272–1278.
40 Y. Xu, J. Wei, L. Tan, J. Yu and Y. Chen, *J. Mater. Chem. A*, 2015, **3**, 7121–7131.
41 X. Zhang, Y. Zhao and C. Xu, *Nanoscale*, 2014, **6**, 3638–3646.
42 S. E. Moosavifard, J. Shamsi, S. Fani and S. Kadkhodazade, *RSC Adv.*, 2014, **4**, 52555–52561.
43 M.-C. Liu, L. Kang, L.-B. Kong, C. Lu, X.-J. Ma, X.-M. Li and Y.-C. Luo, *RSC Adv.*, 2013, **3**, 6472–6478.
44 V. Kumar, S. Matz, D. Hoogestraat, V. Bhavanasi, K. Parida, K. Al-Shamery and P. S. Lee, *Adv. Mater.*, 2016, **28**, 6966–6975.
45 H. Lai, Q. Wu, J. Zhao, L. Shang, H. Li, R. Che, Z. Lyu, J. Xiong, L. Yang and X. Wang, *Energy Environ. Sci.*, 2016, **9**, 2053–2060.
46 H. Jiang, C. Li, T. Sun and J. Ma, *Nanoscale*, 2012, **4**, 807–812.